com baixo contraste, como áreas cobertas por neve e no interior do manto de gelo. O mosaico REMA apresenta para 68º e 90º percentil dos erros (LE68 e LE90) 0,63 e 1,00 metro, respectivamente (HOWAT et al., 2019). A aquisição das imagens que compõem cada tile do mosaico se deu entre os anos de 2009 e 2017, no entanto a maioria das imagens foi adquirida em 2015 e 2016. Os *tiles* de 1^ox1^o são disponibilizados em projeção estereográfica polar entregue com resolução de 8 m. A grade do REMA foi tomada como a grade comum de referência às demais reprojeções e etapas de processamento.

2.2.3 TanDEM-X

Este mesmo modelo descrito na seção anterior foi também utilizado neste segundo artigo, porém com processamento e extensão distintos. A partir do mosaico virtual, uma imagem, cobrindo toda extensão da bacia de drenagem da Geleira Union (limite das bacias glaciais do projeto MEaSURE (MOUGINOT; SCHEUCHL; RIGNOT, 2017)), fora reprojetada para projeção estereográfica polar (EPSG:3031) com reamostragem bilinear e para a grade comum, com 8 m de resolução. As imagens que compõem o TDX foram adquiridas durante o inverno austral, entre maio e julho dos anos 2013 e 2014 (RIZZOLI et al., 2017). Uma avaliação global realizada por estes autores confirmou exatidão absoluta de 3,49 m a 90% de nível de confiança, bem abaixo dos 10 m especificados pela missão. Uma segunda avaliação, a partir de dados de GPS com exatidão inferior a 0,5 m, confirmou um erro ainda menor, inferior a 2 m (WESSEL et al., 2018). Uma vez que estas validações não incluem o continente Antártico, o erro pode ser avaliado pelo mapa de erro de altura (*Height Error Map* - HEM) anotado junto a cada tile do TDX, uma vez que o HEM é uma boa estimativa do erro aleatório teórico (WESSEL et al., 2018).

2.2.4 Análise de acurácia dos DEMs

Os dois modelos digitais de elevação REMA e TDX foram validados com os pontos GPS de alta exatidão. Além disso, os dados de elevação utilizadas referem-se ao elipsóide WGS84 e as diferenças de altitude elipsoidal, calculadas subtraindo-se a altitude do GPS do correspondente pixel do DEM ($\Delta h = h_{DEM} - h_{GPS}$). Cabe lembrar que, os pontos GPS foram transferidos para a posição do pixel mais próximo da grade dos modelos de elevação, portanto a diferença planimétrica não foi considerada.

No respectivo trabalho, interpretou-se e avaliou-se a acurácia da mesma maneira feita por Wessel et al. (2018), em que o erro sistemático é estimado pelo viés estatístico e o erro aleatório, pelo desvio das diferenças de altitude. Excluíram-se diferenças maiores que 3 vezes o desvio padrão antes dos cálculos estatísticos. Considerando uma distribuição normal, estimou-se o erro a partir do cálculo do erro médio (mean error – ME, equação 2.1); o erro quadrático médio (root mean square error – RMSE, equação 2.2); e o desvio padrão (standard deviation – STD, equação 2.3).

$$ME = \frac{1}{n}\sum_{i=1}^{n}\Delta h_i \tag{2.1}$$

$$RMSE = \sqrt{\frac{1}{n}\sum_{i=1}^{n}\Delta h_i^2} \tag{2.2}$$

$$STD = \sqrt{\frac{1}{n-1}\sum_{i=1}^{n}(\Delta h_i - ME)^2} \tag{2.3}$$

Outras medidas para avaliação da acurácia com uma distribuição não normal do erro também foram calculadas, como proposto por Höhle e Höhle (2009), onde $m_{\Delta h}$ é a mediana, i.e. 50% do quantil, além de calculada a mediana do desvio absoluto (*median absolute deviation* – MAD, equação 2.4); a mediana normalizada (*normalized median* – NMAD, equação 2.5); e o desvio absoluto aos 90% do quantil ou, erro linear ao 90° do intervalo de confiança (LE90, equação 2.6).

$$MAD = median_j(|\Delta h_j - m_{\Delta h}|) \tag{2.4}$$

$$NMAD = 1,4826 \cdot MAD \tag{2.5}$$

$$LE90 = \widehat{Q}_{|\Delta h|}(0,9) \tag{2.6}$$

2.2.5 Diferença entre os DEM

O intervalo temporal entre os dois DEM é de 2-4 anos. Rivera et al. (2014) reportam uma mudança de elevação local média, na porção mais estreita do vale central, de -0,012 m a^{-1}, um valor próximo ao erro das medições, o que indica também uma condição próxima ao equilíbrio. A partir de passagens do sensor altímetro a laser ICESat-GLAS entre 2005 e 2009, confirmou-se também não haver mudança de elevação. Por este motivo, compararam-se os dois DEMs, considerando-se haver diferença de elevação da superfície no intervalo de tempo que separa as duas fonte de dado.

Antes de comparar os dois DEM, observou-se um ruído de alta frequência inerente ao produto TDX, devido à penetração do sinal SAR na neve e à irregularidade da superfície e subsuperfície. Em comparação, o REMA representa a superfície de maneira mais suave e sem ruído. Isso porque cada faixa de DEM que é utilizada na composição do mosaico REMA é filtrada e sub amostrada (*downsampled*) para uma grade de 32 m de resolução durante o processo de corregistro com o CryoSat-2 (HOWAT et al., 2019). Portanto, o

TDX foi filtrado com uma média móvel de janela 5x5 pixels (40x40 m) e o resultado, referido como TDX_A5, representou a superfície mais suave similar ao REMA.

Para o mapa de diferenças de altura (figura 1, capítulo 4), subtraiu-se o valor de elevação do REMA do TDX (TDX-REMA). As diferenças de altura, empregando-se o TDX_A5, apresentam áreas mais homogêneas, representando melhor a tendência local de uma área em super ou subestimar a elevação em relação ao REMA.

2.2.6 Áreas mascaradas

Neste segundo artigo, a comparação entre os DEM também foca em zonas cobertas com neve e de declive suave. Desta forma, reduz-se a comparação de áreas com maiores estimativas de erro, diretamente relacionadas a áreas de maior declividade. As áreas de gelo foram mascaradas com o dado poligonal do limite de BIA (Hui et al. 2014). Baseou-se no produto de declividade gerado a partir do REMA para mascarar áreas de declive moderado a alto, isto é, maior que 5^o (10% de declive). As regiões mascaradas podem ser conferidas na figura 1, capítulo 4. A abordagem por meio da declividade possibilitou separar áreas montanhosas (íngremes) e área de rocha exposta e, ao mesmo tempo, reduzir o efeito da geometria no sinal SAR. Para os cálculos estatísticos da acurácia, BIA em áreas com declividade superior a 5°, considerou-as como áreas íngremes.

2.2.7 Dados de GPR

Para a coleta de perfis de GPR utilizou-se um equipamento GSSI SIR® System-3000 com uma antena de 400 MHz com alcance de 150 ns (∼12 m de profundidade em neve seca) para os mesmos 70 km de deslocamento de coleta dos dados de GPS (figura 1, capítulo 4). Coletou-se, também, dados com o alcance de 600 ns (∼60 m de profundidade) no vale central para rastrear a profundidade do *firn* até os 60 m. Todos os perfis foram coletados em modo tempo e não automaticamente sincronizados com dados do GPS, pós processados e exportado em software SIG para georeferenciamento e correção topográfica dos perfis GPR. Analisaram-se perfis nos quais era possível identificar a interface*firn*/gelo e extrair sua profundidade.

3 Capítulo 3 - Artigo 1

O primeiro manuscrito, de autoria de Christian Florian Gobel, Jorge Arigony-Neto, Ricardo Jaña, Rodrigo Gomez-Fell, Jean de Almeida Espinoza, Francisco Fernandoy, Ian D. Goodwin e Gulab Singh, é intitulado **“Snow-deposition characteristics from SAR and geospatial analysis atUnion Glacier, Antarctica"** e submetido na revista *Antarctic Science*

Neste primeiro artigo, analisou-se dados estratigráficos de sete locais da Geleira Union com distintas respostas de retroespalhamento do sinal SAR na banda-X. Foi possível caracterizá-los com relação a um ambiente mais ou menos exposto ao vento. Assim, com o uso de imagens CSK em modo de aquisição Stripmap HIMAGE de 2011/2012, mapeou-se e classificou-se as áreas de cobertura de neve por classes como resultado da interpretação dos dados dos *snowpits*. Ao final, produtos derivados a partir de um DEM foram gerados para melhorar a análise de cluster proposta e a delimitação espacial dos ambientes deposicionais de neve. São apresentadas 6 classes que representam, de maneira qualitativa, áreas de maior ou menor taxa de acumulação de neve.

Snow-deposition characteristics from SAR and geospatial analysis at Union Glacier, Antarctica

Christian Florian Göbel[1] – ORCID: 0000-0002-2646-6437

Jorge Arigony-Neto[1] - ORCID: 0000-0003-4848-2064

Ricardo Jaña[2] - ORCID: 0000-0003-3319-1168

Rodrigo Gomez-Fell[3] - ORCID: 0000-0002-0391-1323

Jean de Almeida Espinoza[4] - ORCID: 0000-0002-7933-2897

Francisco Fernandoy[5] - ORCID: 0000-0003-2252-7746

Ian D. Goodwin[6] - ORCID: 0000-0001-8682-6409

Gulab Singh[7] – ORCID: 0000-0002-7774-5997

[1] Instituto de Oceanografia, Universidade Federal do Rio Grande, Av. Itália km8, CEP 96201900, Rio Grande, RS, Brazil.

[2] Departamento Científico, Instituto Antártico Chileno, Plaza Muñoz Gamero 1055, Punta Arenas, Chile.

[3] Centro Regional Fundacion CEQUA, Av. España 184, Punta Arenas, Chile.

[4] Instituto Federal de Educação, Ciência e Tecnologia do Rio Grande do Sul, R. Eng. Alfredo Huck, 475, Rio Grande, 96201-460, Brazil.

[5] Facultad de Ingeniería, Universidad Nacional Andrés Bello, Viña del Mar, 2531015, Chile.

[6] Department of Environmental Sciences, Macquarie University, Sydney NSW 2109, Australia.

[7] Centre of Studies in Resources Engineering, Indian Institute of Technology Bombay, India.

Corresponding author: Christian Florian Göbel (cfgobel@gmail.com)

Abstract

The Union Glacier in the Ellsworth Mountain Range drains its mass to the Ronne-Filchner Ice Shelf. Mean surface mass balance (SMB) estimates range between 0.16 and 0.33 m water equivalent (w.e.) a^{-1} depending on site location and method. Despite agreement among studies, these studies did not represent the high spatial variability in snow deposition dynamics that is caused by relief, wind transport-driven accumulation, and high sublimation rates. A better understanding of these processes is required to improve SMB estimates. In this study, we focus on influence of terrain. We use COSMO-SkyMed SAR, high-resolution TanDEM-X-derived products and field data to identify and delimit zones of distinct accumulation characteristics. Wind-exposed areas have larger snow grains, faceted forms because of longer temperature-gradient exposure, more layers and greater hardness. We run a cluster analysis to classify the depositional zones, and we assess the spatial variability by using a qualitative approach. A high masked-area percentage of 40% indicates that the mean SMB may not adequately represent significant areas. On the other hand, other works may have underestimated the accumulation rate because these studies focused on wind-exposed areas, and higher accumulation rate occurs, for example, inside valleys that are protected from the prevailing wind direction.

Keywords: surface relief; terrain analyses; backscattering; snow accumulation; snowpits; Ellsworth Mountain;

1. Introduction

Antarctica has a vital role in regulating the global climate. The complexities of heat exchange and the interaction of ice shelves and land ice with the ocean and atmosphere make climate-change prediction challenging. The precise quantification of the incoming and outgoing mass is essential to accurately estimate the imbalance of Antarctic glaciers. The quantification of ice losses by dynamic processes has been advanced, but the gain in mass processes, i.e., SMB, remains challenging at finer resolutions. The accumulation processes in Antarctica are highly variable and controlled by regional patterns of precipitation variability; these patterns are driven by large-scale atmospheric moisture transport (Fyke *et al.* 2017). Estimates of the surface mass balance (SMB) in Antarctica that are derived from in-situ data and regional climate models (Arthern *et al.* 2006, van de Berg *et al.* 2006) can introduce a high level of uncertainty into the prediction model because of the coarse resolution.

Snow-accumulation patterns are climate dependent and influenced by topographic settings. Elevation and topographic solar radiation, slope, and aspect regarding the influence of terrain orientation on prevailing wind can be used to predict the variability of this mass-balance component (Böhner & Antonić 2009). Other parameters must also be considered, such as the curvature and catchment area (Böhner & Antonić 2009). Over glacierized areas in complex terrain, modelling the wind field and related variables, such as the aspect and sine of the slope, is a critical factor to understand the mass-balance distribution of glaciers (Dadic *et al.* 2010, Fassnacht *et al.* 2013). Goodwin (1990) showed a strong dependence of the accumulation on the aspect, where synoptic and orographic processes are the dominant controls of the depositional regime. The windward slope has a higher accumulation rate than the leeward slope. Frezzotti et al. (2004, 2007) showed that the slope along the prevailing wind direction considerably affects the spatial distribution of snow over short and medium spatial scales, so the accumulation pattern reflects the surface roughness. Ding et al. (2015)

suggested that one stake alone is insufficient to obtain a mean local SMB value, and comparing the SMB at each stake with the average value across a group of stakes can illustrate the spatial variability of the SMB on a local scale. Ding et al. (2015, 2017) also evaluated the variability of snow accumulation and found that at least 12 and 20 sites are required for local and regional studies of SMB, respectively. On the Antarctic Plateau, wind transport drives the accumulation of snow, and studies have demonstrated the importance (Groot Zwaaftink *et al.* 2013) and quantified the influence of this phenomenon in processes such as sublimation and erosion (Frezzotti *et al.* 2004). These studies demonstrated that snow accumulation cannot be directly related to precipitation events and that better accumulation rate results are obtained by using additional criteria, such as wind-speed conditions, to redistribute the snow. Precipitation estimates that are obtained as residuals from atmospheric water-balance equations are reliable for seasonal time scales and areas of at least 106 km^2. Ding et al. (2017) emphasized the need to consider the snowdrift effect on SMB, which can disturb snow deposition and have up to an 85% effect on the surface mass balance because of wind-driven sublimation.

The Ellsworth Mountains are the boundary between the plateau and grounding line but are located far from the ocean coast because of the Ronne Ice Shelf. The amount of accumulation is moderate in the UG region and does not appear to be directly related to the elevation or distance from the ocean (Hoffmann et al. ‘in review’). Furthermore, spatially varying accumulation trends likely reflect the strong influence of site-specific characteristics on accumulation rates and, in particular, the different exposures to wind drift. Additionally, no apparent correlation exists between the elevation and accumulation. We expect that terrain characteristics such as slope and wind exposure will dictate different depositional zones in these Alpine-like complex topographic areas. In this study, we aim to indirectly infer the spatial variability in snow deposition in an area where the wind field is an essential variable in the study of snow cover, but in which insufficient data and modelling resources limit dynamic modelling.

1.1. Radar use for surface mass balance and correlation

Synthetic aperture radar (SAR) imagery has been widely used for polar science mainly because SAR imagery can acquire images through cloud cover and does not depend on daylight. Within the field of glaciology, SAR imagery can be used to make DEMs to measure glacier velocity, and SAR's ability to penetrate below the glacial surface enables us to detect changes in glacial facies and snow accumulation. These high levels of interaction and dependence on snowpack characteristics occur because the radiation reflection from a planar snow surface is controlled by the incident angle and dielectric constant of the snow. The higher the difference between snow and air, the higher the reflection coefficient becomes. The imaginary component of the dielectric constant, which determines the absorption, is small for dry snow and exhibits some dependence on temperature. Therefore, snow behaves as a quasi-transparent medium, and significant scattering occurs in the snowpack bulk (Rees 2005, section 4.2.6). For example, Forster et al. (1999) used the C-band to show that both the accumulation rate and temperature can modulate surface backscattering across Greenland's dry-snow zone, with the accumulation rate being the primary influence. These researchers also showed that the surface backscattering contribution decreases with increasing incident angle; at 30º, the surface backscattering contribution is close to 100% volume scattering.

The C-band (4 to 8 GHz) and X-band (8 to 12.5 GHz) are commonly used by SAR satellites for snow-cover investigations in dry polar climates. Investigations of snow accumulation that employ backscattering perform better in dry snow, where no water content exists in the liquid state, because of high signal absorption. Electromagnetic radiation at these wavelengths interacts with the snowpack up to 20 and 10 m for the C- and X-bands, respectively (Rott *et al.* 1993). For higher frequencies, the attenuation length decreases exponentially, reducing volume scattering and thus reducing the interaction with the snowpack and its physical properties (Rees 2005, section 4.2.6). The COSMO-SkyMed (CSK) mission operates in the X-band and has been shown to be suitable for dry-snow studies, accomplishing snow water-equivalent retrieval and a good interaction with snowpack properties, such as the crystal size (Pettinato *et al.* 2013). The snowpack stratigraphy results in a specific backscattering signature that can be related to parameters such as density, accumulation rate, snow-grain size, and water content.

Common applications that correlated SAR backscattering and snow-cover properties focused on snow depth (Shi & Dozier 2000) and snow accumulation (Forster *et al.* 1999, Arthern *et al.* 2006, Dierking *et al.* 2012). Few studies correlated SAR backscattering with the physical properties of snow, such as density, grain size and layering, although a reasonable relationship exists among these factors. The accumulation rate controls the evolution of the snowpack (metamorphism) by determining the residence time in the region near the surface and is influenced by the seasonal change in the temperature-depth profile. This result will control the grain-size depth profile. Annual layer thickness and density profiles are also derived from the accumulation rate (Forster *et al.* 1999).

Furthermore, temperature variations must be considered because temperature variations directly increase emissions. Forster et al. (1999) constructed a coupled snow metamorphosis-backscattering model that showed that both the accumulation rate and temperature could modulate surface backscattering across Greenland's dry-snow zone, with the accumulation rate being the primary influence. Generally, backscatter is more sensitive to changes in the accumulation rate when the accumulation rate is low, at 10-25 cm a^{-1} water equivalent (w.e.). Backscatter is a less sensitive indicator of the accumulation rate when the accumulation rate is high.

1.2. Study area

Union Glacier is one of the major outlet glaciers of the southern Ellsworth Mountains, which are called the Heritage Range, on the western Antarctic Ice Sheet. The glacier drains its ice into the Constellation Inlet, which is a component of the Ronne-Filchner Ice Shelf. Union Glacier has a total length of 86 km from the upper divisor with the Institute Ice Stream to the grounding line at Constellation Inlet, with an area of almost 3000 km2 (glacier basin delimited by using the TanDEM-X digital elevation model). The glacial valley is oriented southeast-northwest with several small tributaries draining into the valley. One of the first studies on the glacier's dynamics based on stakes suggested a near steady state and estimated an equilibrium net mass balance, as inferred from an ice flux model, equivalent to an accumulation of 0.13-0.23 m w.e. a^{-1} (Rivera *et al.* 2010), which neglected sublimation at the glacial surface. Similar values of balance accumulation were obtained by Wendt et al. (2009) for Horseshoe Valley to the southwest of Union Glacier. (Rivera *et al.* 2014) confirmed near-equilibrium conditions and a mean accumulation of 0.3 m a^{-1}, or 0.12 m w.e. a^{-1}, considering a mean snow density of 400 kg m^{-3}. Rivera et al. (2014) found a maximum net balance of 0.2 m w.e. a^{-1} for a specific point, i.e., stake B12, downstream from the Blue Ice Area (BIA). This stake is located close to our automatic weather station (AWS). Other accumulation estimates that were derived from regional atmospheric climate models (van de Berg *et al.* 2006) and the interpolation of field data (Arthern *et al.* 2006) ranged between 0.16 and 0.33 m w.e. a^{-1}. Work on firn core samples that were collected from six sites in the Union Glacier region generally showed annual minimum accumulation ranges between 0.1 and 0.2 m w.e. a^{-1} and maximum annual accumulation values of ≥ 0.3 m w.e. a^{-1} (Hoffmann et al. 'in review'). Although these studies showed agreement, these studies did not depict the local variability in snow accumulation that was caused by surface microrelief and variable wind fields or distinct densification processes. For example, Hoffmann et al. ('in review') also found an absolute maximum of 0.47 m w.e. a^{-1} and an absolute minimum of 0.08 m w.e. a^{-1} for the same year at different sites. These researchers concluded that the spatially varying accumulation trends of the drilled sites were mainly related to wind exposure (Hoffmann et al. ‘in review’). This variability was also observed in the variance in the specific mass balance between stake measurements (Rivera et al. 2014). Therefore, this parameter can affect the SMB, which will subsequently affect the mass balance budget of the glacial drainage basin. We believe that the specific study area represents the spatial variability of the accumulation dynamics of the entire Ellsworth Mountain Range, which has not been addressed in climate models.

In this paper, the spatial variability of snow accumulation is investigated in contrasting deposition environments on Union Glacier in the Ellsworth Mountains. We sampled seven sites with distinct SAR X-band backscattering signals, with stratigraphic analyses in 2-m snowpits. We were able to characterize the signals in terms of more or less exposure to wind. Then, we mapped and classified the snow surface area based on the interpretation of the snowpit data by using CSK Stripmap Himage acquisition modes from 2011/2012. Finally, we derived surface products from a DEM to improve the cluster analyses and spatial delimitation of snow depositional environments. We characterized these environments into six classes that represented higher and lower accumulation rates. Further work will analyse the shallow ground penetrating radar (GPR) profile across the glacier to identify differences in accumulation rates.

2. Data and methodology

2.1. AWS and Snow Depth

We installed an AWS UNION13 in 2013 (79º46.22’ S, 82º54.72’ W, 693 m asl) at the windward side of the Chilean base camp Estación Polar Científica Conjunta Glaciar Union (EPCCGU). We collected basic weather parameters (i.e., surface air temperature, snow temperature, atmospheric pressure and humidity, solar radiation, and wind direction and speed), and we installed a sonic sensor (SR50) to build a snow-depth time series. The AWS registered hourly averaged parameters alongside some hourly minimum and maximum values. The snow-depth sensor recorded 2-min measurements every hour to save battery power. The hourly data were sent to a web link through an iridium modem. Other parameters, such as the hourly deviation, minimum and maximum, were recovered from the data logger only once a year. In 2015, we installed a second station on a small tributary called Criosfera Glacier (unofficial name) or Rossmann inlet (black rectangle in Figure 1).

2.2. Snowpits

Almost simultaneously during image acquisition, we dug seven snowpits (SP), which were spread throughout the glacial valley (Table I). We chose the locations based on different backscattering values of a coloured cross-polarized composition (R: VV-VH; G: VH; B: VV) by using the CSK Ping Pong from July 2011 preceding the field work (Figure 1). The snowpits followed the necessary procedure that is adopted by most mountain-station agencies, which is 2-m depth, records of the grain type and size, hand-hardness values for each layer, and temperature and density measurements for each 10-cm interval. We also took pictures of the surface characteristics of the areas surrounding the snowpits. In our campaign, we did not systematically record the microrelief in each SP, but we took pictures of the surrounding surface characteristics to compare with the descriptions from Goodwin (1990) and the well-documented pictures from Fujiwara & Endo (1971). Goodwin (1990) correlated surface topography with accumulation in a katabatic zone in the eastern Wilkes Land. He focused on the mesoscale in the study, considering the factors that influence snow accumulation beyond the strong correlation with elevation at a broad scale. In the katabatic zone, the net snow accumulation at a given point is a function of both the precipitation that is received at that point and the amount of drifting snow that is redistributed at that point. The amount of drifted snow that is deposited or eroded by wind redistribution is controlled by the local surface roughness and its effects on wind turbulence and speed. The wind speed is controlled by the regional maximum surface slope (Goodwin 1990). The classification system that was used by Goodwin was described by Fujiwara & Endo (1971) and applied during Japanese Antarctic Research Expedition (JARE) traverses inland of Syowa on the Mizuho Plateau region of Queen Maud Land.

Table I: Dates that the seven snowpits were dug and the current locations and elevations above sea level (extracted from the digital elevation model that was used in this study).

Snowpit name	Digging date	Latitude	Longitude	Elevation (m asl)
SP1	31-12-2011	-79.779	-83.066	720
SP2	29-12-2011	-79.765	-82.958	697
SP3	02-01-2012	-79.729	-82.774	659
SP4	04-01-2012	-79.736	-83.004	672
SP5	06-01-2012	-79.709	-82.882	669
SP6	07-01-2012	-79.676	-83.216	729
SPA	19-12-2011	-79.761	-82.834	678

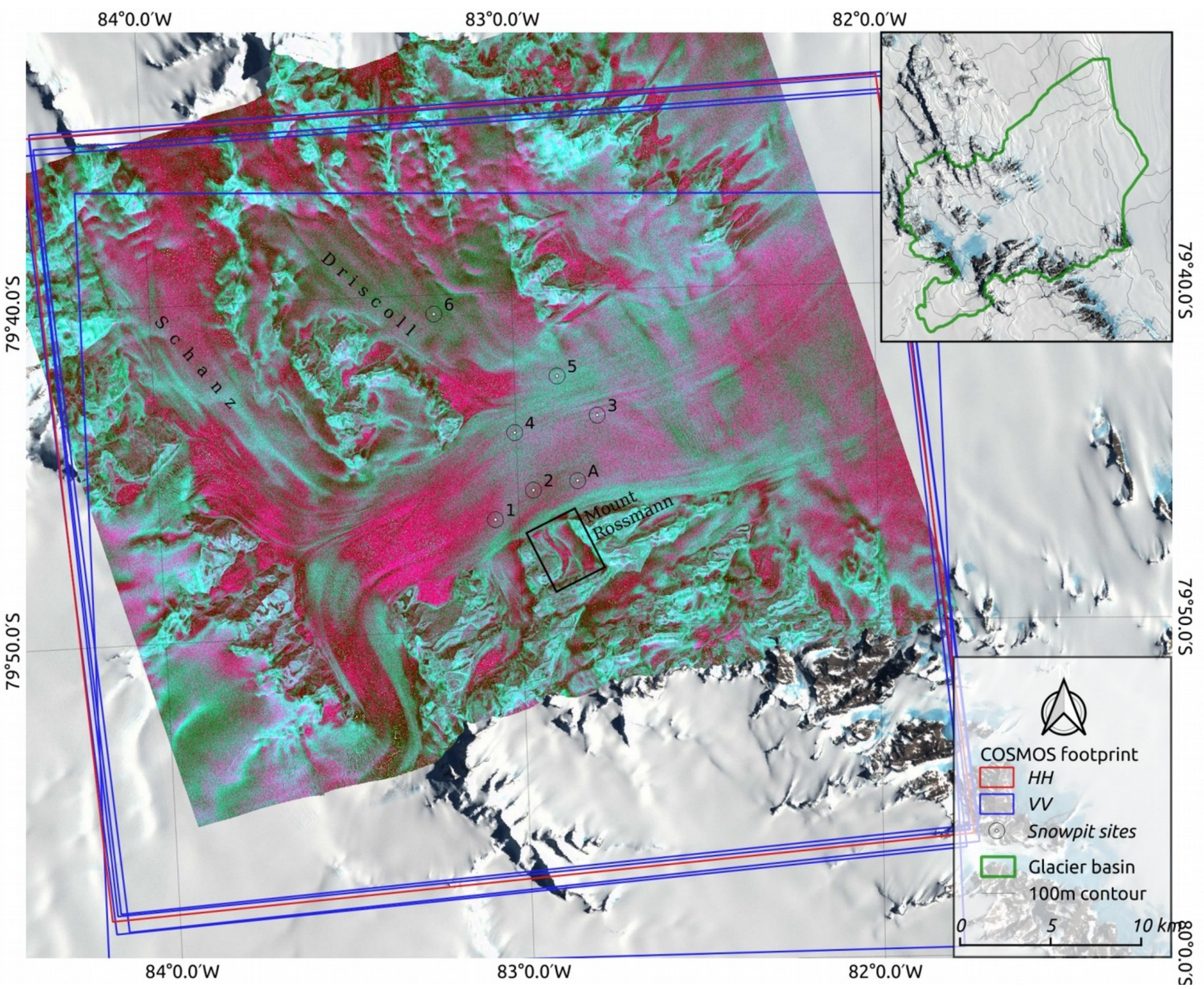

Figure 1: The coverage areas of the six CSK Stripmap Himage VV and HH images are delimited by blue and red polygons, respectively. The one blue polygon that is offset from the others corresponds to the winter image. The coloured image is the Ping Pong acquisition mode cross-polarized composition (R: VV-VH; G: VH; B: VV). The target points show the locations of the

seven snowpits. The insert map shows a delimited overview from the entire Union Glacier Basin. The background image is the LIMA Mosaic.

2.3. SAR and DEM

CSK is a constellation of four satellites with an X-band (9.6 GHz) SAR sensor that was launched by the Italian Space Agency (ASI). The images were obtained through an ASI announcement of opportunity for scientific purposes under the project “COSMO-SkyMed data in support of climate sensitivity studies of selected glaciers in Antarctica, South America, the Arctic and Northern Europe (GlacioCOSMO)”; see Table II for the image specifications. We used the Ping Pong composition (R=VV-VH, G=VH, B=VV) to select the seven snowpit locations, covering sites with distinct backscattering patterns (Figure 1). The five Himage VV polarized images were radiometrically calibrated, speckle filtered and terrain corrected by using TanDEM-X and projected into the UTM projection. For each image, we applied an algorithm to generate maps of the physical characteristics of the snowpack, including the density and grain size. The equations were based on the inversion of a radiative transference model (RTM) (Espinoza *et al.* 2014). This model describes the X-band SAR backscatter in the snowpack as a function of one variable while parameterizing the other snowpack parameters (i.e., varying only the modelled parameter). Generally, high backscattering values are associated with either a higher snow density or small grain size. Although Espinoza et al. (2014) did not quantitatively validate the algorithms, we used these algorithms in a qualitative approach.

Table II: Characteristics of CSK images that were acquired through the Italian Space Agency's announcement of opportunity. The reference incident angle of all the images is 40º, but the Tie-Point Grid exhibits incident angles that range from 22º to 26º for Himages and 19º to 22º for Ping Pong.

Imaging mode	Date of acquisition	Polarization	Pass	Satellite number	Side of looking
Himage	14-07-2011	HH	Descending	2	Right
Himage	14-07-2011	VV	Descending	3	Right
Himage	21-12-2011	VV	Descending	3	Right
Himage	14-01-2012	VV	Descending	1	Right
Himage	22-01-2012	VV	Descending	2	Right
Himage	30-01-2012	VV	Descending	1	Right
Ping Pong	14-07-2011	VH-VV	Descending	3	Right

We stacked the five VV polarized images to match the grid position and resolution by using bilinear resampling, and we calculated the mean backscattering values for each pixel. The five VV polarized CSK images exhibited small differences, with a ~1.1 mean standard deviation that excluded masked areas (Figure 2). We tested the images while excluding the VV winter image, but the standard deviation did not improve (blue line in Figure 2). Thus, these differences occurred between winter and summer and between summer images, possibly because of snow deposition, changes in surface relief and changes in acquisition geometry. Additionally, a portion of this variance was caused by speckling, which is inherent to SAR images. We neglected the difference considering an (i.) X-band attenuation depth up to 8 m (Hofer & Mätzler 1980, Rott *et al.* 1993), (ii.) maximum surface-height change at 60 cm, and (iii.) dominant volume scattering contribution and neglected surface reflection because of a greater incident angle and small dielectric contrast (Forster *et al.* 1999, Du *et al.* 2010, Dierking *et al.* 2012). The density and grain-size maps were calculated for each image and then averaged. Finally, we downscaled to a single median map with a resolution that was compatible with TanDEM-X (12 m) and applied a median filter with a kernel size of 3x3 for smoothness. The five stacked images covered 1620 km² of the central valley of the glacier, with all the images overlapping (Figure 1).

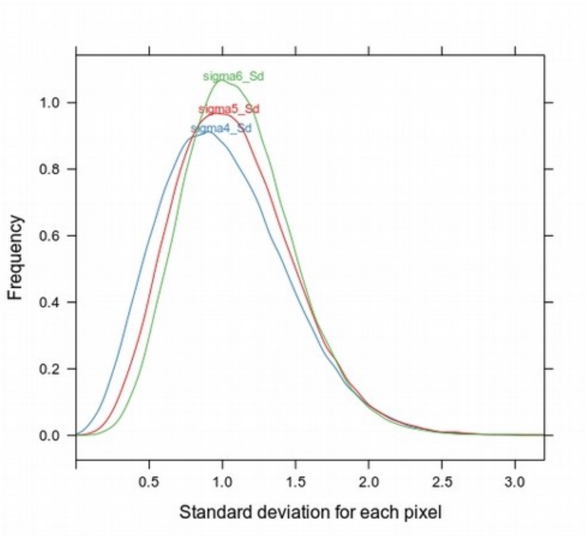

Figure 2: Histograms that compare the standard deviations of the averaged images using only the four summer VV Himages ('sigma4_Sd' in blue), the four summer VV and one winter VV Himage ('sigma5_Sd' in red), and all six Himages including the winter HH ('sigma6_Sd' in green).

In the BIA, the backscattering behaviour changed and lower volume and higher surface scattering occurred because of the dielectric properties of the ice. The rocky areas also reproduced a particular backscattering behaviour because of the exposed rock or specular geometry scatter of the sloped surface. We masked these areas to focus our analyses and classification of the deposition zone on the snowpack. We used polygon data that represented the limits of BIAs (Hui *et al.* 2014) and rocky areas (Burton-Johnson *et al.* 2016) from the SCAR Antarctic Digital Database, all of which is available from the Quantarctica GIS Project. We manually edited a final mask polygon, selecting the snow-covered valley area for study.

The TanDEM-X tiles were obtained through the German Aerospace Center (DLR) call for proposal "TanDEM-X data in support of glacier mass balance and remote sensing studies of glaciers in Southern Patagonia and Ellsworth Mountains (Antarctica)". The DEM was delivered in 1ºx1º tiles in a geographic coordinate system with 1 arcsec of resolution in latitude and 3 arcsecs in longitude at high latitudes, which corresponds to an ~6x12-m resolution for the study area. The DEM was designed with global accuracies of at least 10 m for the absolute height error, but (Wessel *et al.* 2018) found that the absolute height error was less than 2 m. Most terrain-analysis algorithms require a regular grid and metric distance to calculate the terrain characteristics. Therefore, a subset of TanDEM-X was re-projected to a UTM projection with a regular 12-m grid by using bilinear resampling. To improve the cluster classification, we derived slope, aspect, roughness and wind-effect data from the DEM by using the terrain-analysis algorithms in QGIS v.3. A median filter with a 5x5 window size was applied to each product for smoothing, and better results were obtained for the cluster analysis.

The slope product resulted in high variability because the DEM reflects small-scale (<12 m) surface features. Thus, even in flat or low-slope areas, the maps showed values between 1º and 2º, which represent a rough surface. Because we intend to assign more weight to a lower range of values, we applied a nonlinear transformation by taking the cube root, similar to Plattner et al. (2004) for the curvature parameter.

We converted the aspect to the relative land-surface aspect $\boldsymbol{\alpha}_r$, i.e., the absolute value (º) of the angle distance from the terrain aspect $\boldsymbol{\alpha}$ to the azimuth of the prevailing wind direction (Plattner et al. 2004, Böhner & Antonić 2009). We expressed this value as $\cos(\boldsymbol{\alpha}_r)$, where 1 corresponds to a windward aspect and -1 to a leeward aspect.

Plattner et al. (2004) observed that for low curvature values a small change has a significant effect on accumulation, while for high values, a small change does not have a further impact. Therefore, we extracted the cubic square root from values because the relationship is not linear, following the same logic for roughness values (Plattner et al. 2004).

We used the SAGA GIS wind-effect algorithm, referring to Winstral et al. (2002). One can insert a wind-direction grid or consider a mean wind direction for an entire elevation grid. Böhner & Antonić (2009) suggested using various distances and different directions to choose the direction or distance that shows the greatest ability to explain the spatial variability of the targeted phenomenon. We tested wind-effect maps by using either of two different mean wind directions as input: 225º or 255º.

2.4. Cluster classification

We performed a cluster analysis to semi-automatically classify the different depositional zones. Clustering is commonly used for exploratory data mining in many fields, such as machine learning, pattern recognition, image analysis, information retrieval, bioinformatics, data compression, and computer graphics. Clustering involves grouping together a set of objects, in this case, the pixel values, in a manner that objects in the same cluster are more similar to each other than to objects in other clusters. The k-means method interprets this similarity as the Euclidean distance from each pixel's value to each centroid and the deviation that defines a cluster group. In the k-means cluster partition, each element is placed into different groups. The k-means cluster partition runs successive interactions, minimizing the square root error of each group and in each interaction by adjusting the centroid of each group. We used the “k-means clustering for grids” module from SAGA GIS, alongside the Minimum Distance/Hill Climbing method, data normalization and maximum interactions.

We defined six classes based on practical recommendations of the number of expected classes times two (*2) because we wanted to obtain three classes: low, medium and high accumulation-rate zones. We used the elbow method to confirm this number, computing the sum of the squared errors for all pixels in the varying numbers of classes in the clustering analysis. When plotted, the idea is to find the elbow point where increasing k produced little return. We evaluated the elbow method with only the averaged sigma-ø image as the dataset. The plot did not present a clear elbow point (Figure 3a.), suggesting between four and six classes.

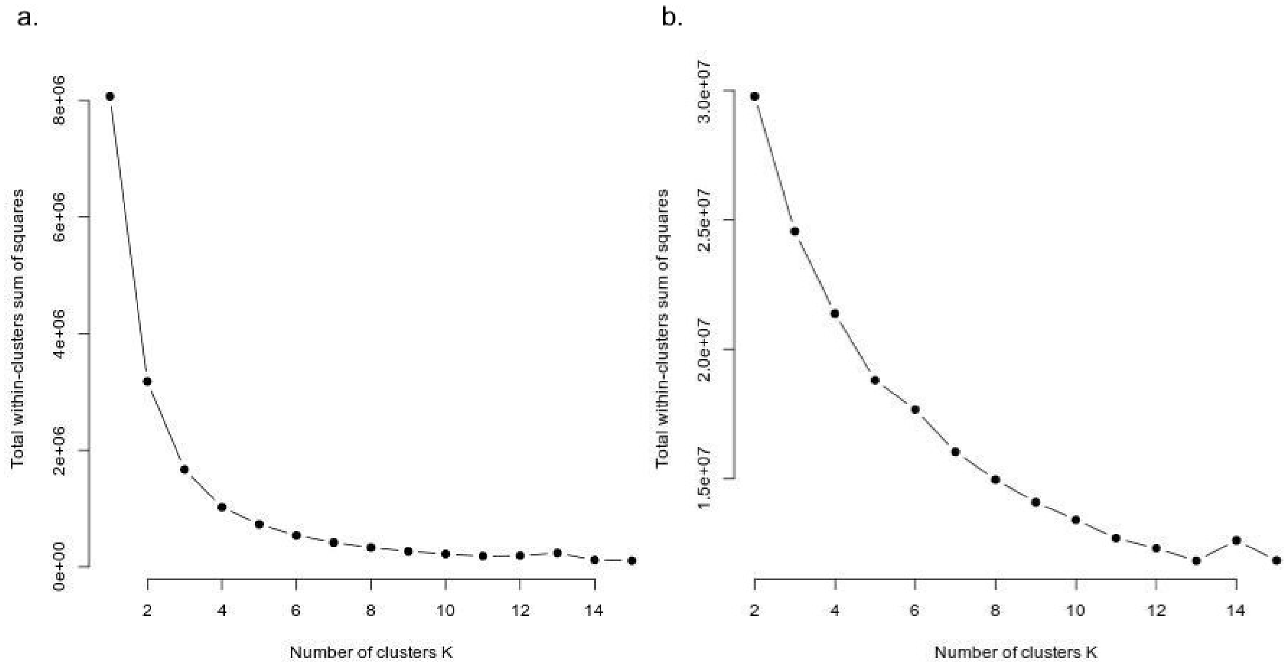

Figure 3: (Left) Plot of the sum squared error (SSE on the y-axis) for all the pixels in the clustering analysis with only the averaged sigma image as input and the number of cluster groups k (x-axis). (Right) Same plot for the clustering analysis with the averaged sigma image and all the terrain products that were derived as input. The elbow method suggests that the number k should be at the point where increasing k provides little return when decreasing the SSE.

For this reason, we also performed classifications with four and five classes and evaluated the distinct generated zones that matched the classification of each snowpit through visual interpretation. We ultimately used six classes. In addition, the elbow method showed that the curve became less steep when more variables were added to the dataset, and no good elbow point was defined (Figure 3b.). We decided to keep six classes to better compare the results to the classification without terrain products as input. We also explored the relationship of each terrain product to the sigma in a hexbin scatterplot (Figure S8), except for (e), which is the slope against roughness. We observed no explicit variable with unique groups of values, but the roughness, slope, and elevation showed some grouping in their point clouds. We plotted an elbow graph with four variables (roughness, slope, elevation, and sigma). The results did not present an apparent elbow. Instead, two break points appeared at five and seven classes (Figure S9; see the scatterplot section in the attached material).

3. Results

3.1. AWS and Snow Depth

The data from the AWS installed in December 2013 showed total annual accumulations of 0.225 m w.e. for 2014 (mean density of 364 kg m^{-3} for the first 0.6 m of the snowpit from 26 November 2014), 0.192 m w.e. for 2015 (mean density of 406 kg m^{-3} for the first 0.3 m of the snowpit from 3 December 2015), 0.150 m w.e. for 2016 (mean density of 365 kg m^{-3} for the first 0.4 m of the snowpit from 26 November 2016), and 0.104 m w.e. for 2017 (mean density of 375 kg m^{-3}, averaged from other years) (Figure 4).

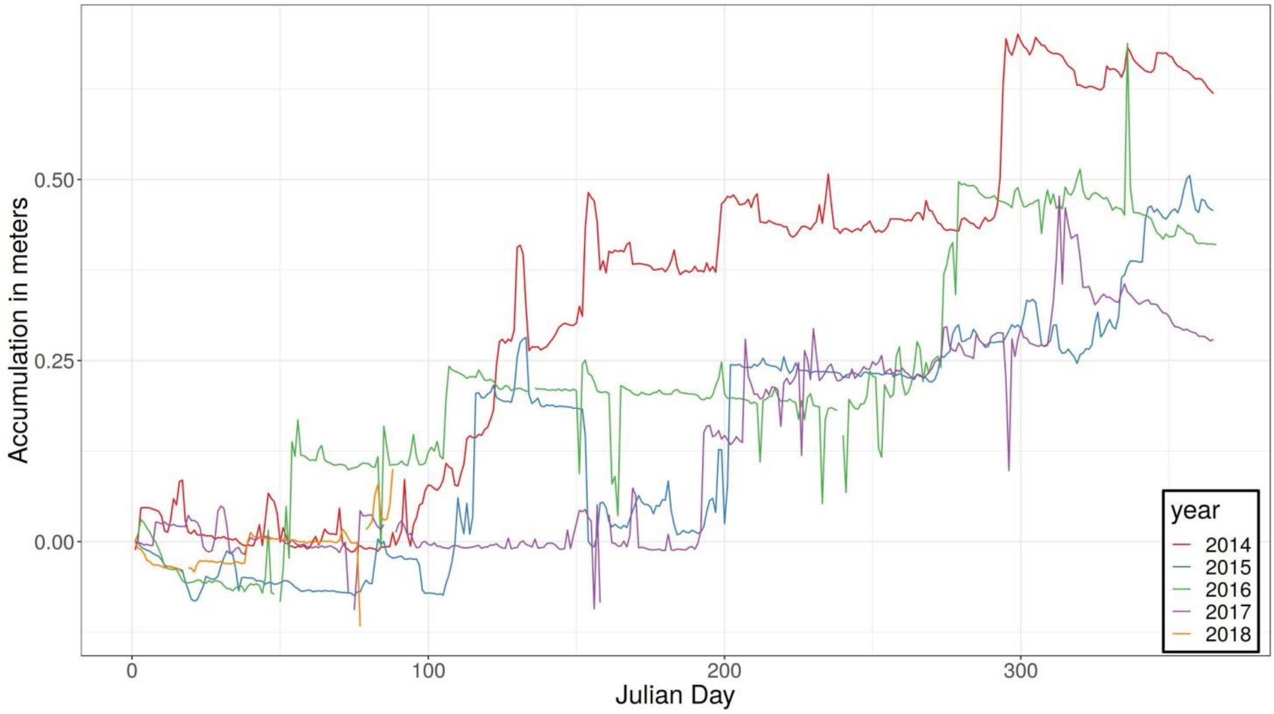

Figure 4: Annual surface heights from the sonic sensor (SR50) at the Union13 AWS from 2014 to 2017. For comparison, the surface was set to 0 m for each year. No annual cycle was present, and the net accumulation occurred in specific events, mainly during spring and autumn.

During these four years, the predominant wind direction was SW (255º), with mean annual wind speeds of 3.32 m s^{-1} (2014), 3.88 m s^{-1} (2015), and 4.01 m s^{-1} (2016). The mean annual temperature was -21.68 ºC (2014), -22.07 ºC (2015) and -20.76 ºC (2016).

3.2. Snowpit

Stratigraphic analyses of the seven snowpits from the 2011/2012 fieldwork were conducted by the same analysts to reduce errors in misinterpretation. With different characteristics, SP1 and SP4 showed more layers and consistently faceted crystals (Figure S1 and Figure S4). Generally, each layer was thin and mostly exhibited knife hardness, indicating proper compaction. The grain sizes were higher, ranging mostly between 1 and 4 mm and may have been larger in some layers. Generally, SP1 had the largest sizes. The two site locations are well known from field experience to be highly exposed to wind, so we assumed a depositional zone with persistent wind that sporadically received drifted snow from the Antarctic Plateau.

Snowpit A (SPA) demonstrated the most complex stratigraphy, with twice as many layers as SP2, which was only a few kilometres away (Figure S7). This particular location close to Mount Rossman probably blocks the prevailing SW wind. This fact could explain most of the irregular, small grain-size forms (i.e., mechanically broken fragments), which probably overcome this topographic obstacle. Some rounded forms also occurred. Faceted grain types also appeared, probably because of the low amount of deposition (i.e., thin layers) with more time exposed to the wind and temperature gradients.

Snowpit 3 was in the central portion of the Union Glacier valley and downslope from the katabatic winds. Snowpit 3 was less than 5 km downward from SP4 and had a regular frequency of layering that was similar to SP4. In the first meter of depth, the snowpits corresponded in terms of layering. In SP3, the soft layers were thicker, whereas the hard layers were thinner, which indicates a more intense densification process in SP4. SP3 had only a few layers as hard as those in SP4, but the layers were thinner (Figure S3). The described difference was apparent in the first 60 cm of depth. The density profiles of both snowpits had some corresponding inflection points, which were probably similar deposition events because the snowpits were close to each other and under the same influence of katabatic wind from the plateau (Figure 5). The offset between the first inflection of maximum density was approximately 10 cm (at 140- and 130-cm depths), which could indicate the difference in accumulation rates between the two locations. Considering the crystal forms, SP3 presented rare faceted crystal forms, and only in three layers. Most of the layers intercalated from irregular and rounded forms, indicating mixed sources from precipitated and wind-transported snow. The layers were thicker than those in SP4. The snow-grain sizes were mostly approximately 1 mm along the first meter and larger (>2 mm) in the softer layers of the second meter.

Finally, snowpit 5 (SP5) stratigraphy indicated a higher accumulation zone, similar to SP2 and SP6, but with the frequent occurrence of faceted crystal forms (Figure S5). The latter form occurred in softer layers with large grain sizes (i.e., >3 to 8 mm), intercalating harder layers of smaller grain sizes with rounded forms. Most of the grains were also irregular forms. Similar to SP3, this zone is probably influenced by mass deposition by wind transportation (rounded grains), as in Driscoll valley but with larger grain sizes; simultaneously, redistributed blowing snow drifted from the upper central valley (irregular form) from local precipitation.

We summarize the interpretation of the seven snowpits in Table III. We expect that zones of lower accumulation and within more wind-exposed areas will show (i.) more layers, which are thinner and harder; (ii.) generally larger grain sizes (1 - 4+ mm); and (iii.) frequent faceted crystals because of higher temperature-gradient metamorphism.

Table III: Summary of the snowpit characteristics. "Numbers of layers" corresponds to the total layers that were visually identified in the 2-m-deep snowpits. The mean density is the average 10-cm interval density of the first 2 m. The dominant hardness is the visual interpretation of the hand hardness estimation. The classification of surface relief was conducted through interpretations of pictures of the areas that surrounded each snowpit. The supplementary material displays stratigraphic graphs of each snowpit, which were produced in the Snowpilot software.

Snowpit	Number of layers	Mean density (kg m^{-3})	Dominant hardness	Dominant grain size (mm)	Crystal form	Classification of surface relief
1	19	433	Harder	2.0-3.0+	Faceted-irregular, some rounded	Erosional features
2	14	417	Softer	0.5-1.0	Irregular, little rounded	Depositional features
3	24	375	Softer	0.5-2.0	Irregular-rounded, little faceted	Redistribution features
4	22	400	Harder	1.0-3.0+	Faceted-irregular, little rounded	Erosional features
5	19	404	Medium	1.0-2.0+	Rounded-irregular, some faceted	Redistribution features
6	16	388	Software	0.5-1.5+	Rounded-irregular	Depositional features
A	38	373	Harder	0.3-1.0	Irregular-faceted, little rounded	Depositional (low rate)

The snow-density profiles indicated differences in the variance between layers on the southern side (i.e., SP1, SP2, and SPA) and the northern side of the valley (i.e., SP3 to SP6) (Figure 5). We note higher density values in SP1 and SP2 and a higher range. Both snowpits had similar density profiles, which were slightly offset, with SP2 deeper in the first meter, although the second meter was as shallow as that in SP1.The snowpit graph showed fewer but thicker layers in SP2, while SP1 had multiple layers of the same hardness, indicating a more wind-exposed zone, which accelerated the process of differentiating layers.

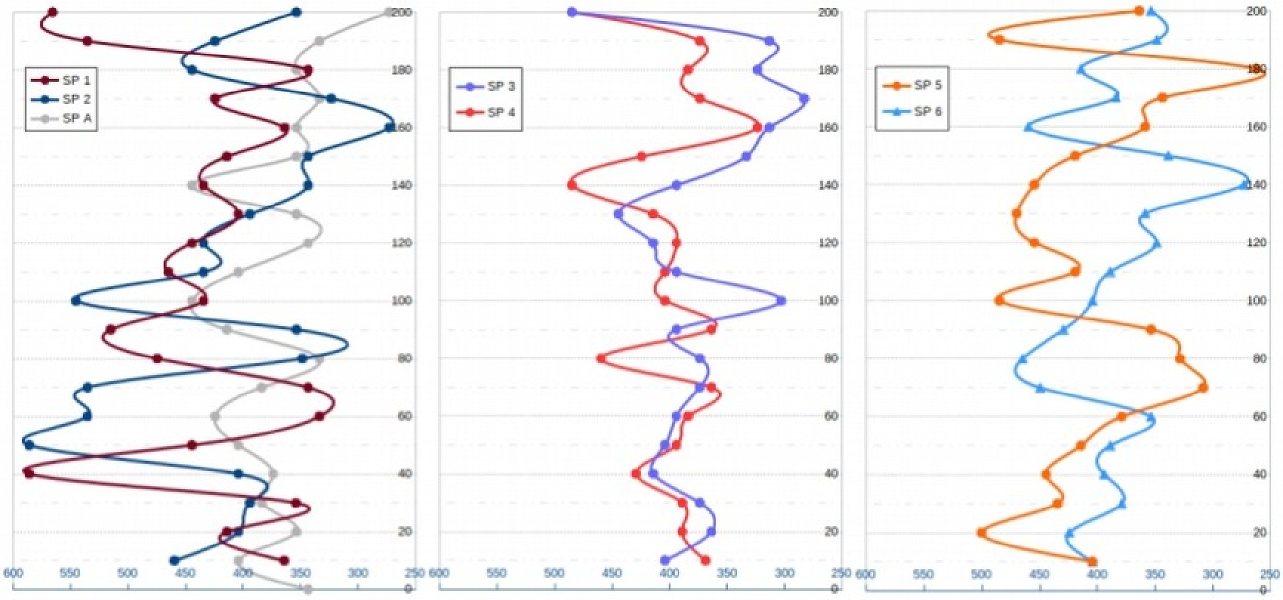

Figure 5: Density profiles from each snowpit. We separated the profiles by proximity and clarity. The axes are on the same scale and in the same range.

The interpretation of the surrounding area's pictures corroborated and reinforced our interpretation of each snowpit. We classified each snowpit into one of three surface microrelief types: (i) stationary depositional features that formed during precipitation (SP6 and SP2, Figure 6e. and 6f.), (ii) mobile depositional or re-distributional features that formed from wind-transported friable snow (SP5 and SP3, Figure 6c. and 6d.), and (iii) erosional features that formed from long-term exposure to katabatic winds during hiatuses in precipitation (SP1 and SP4, Figure 6a. and 6b).

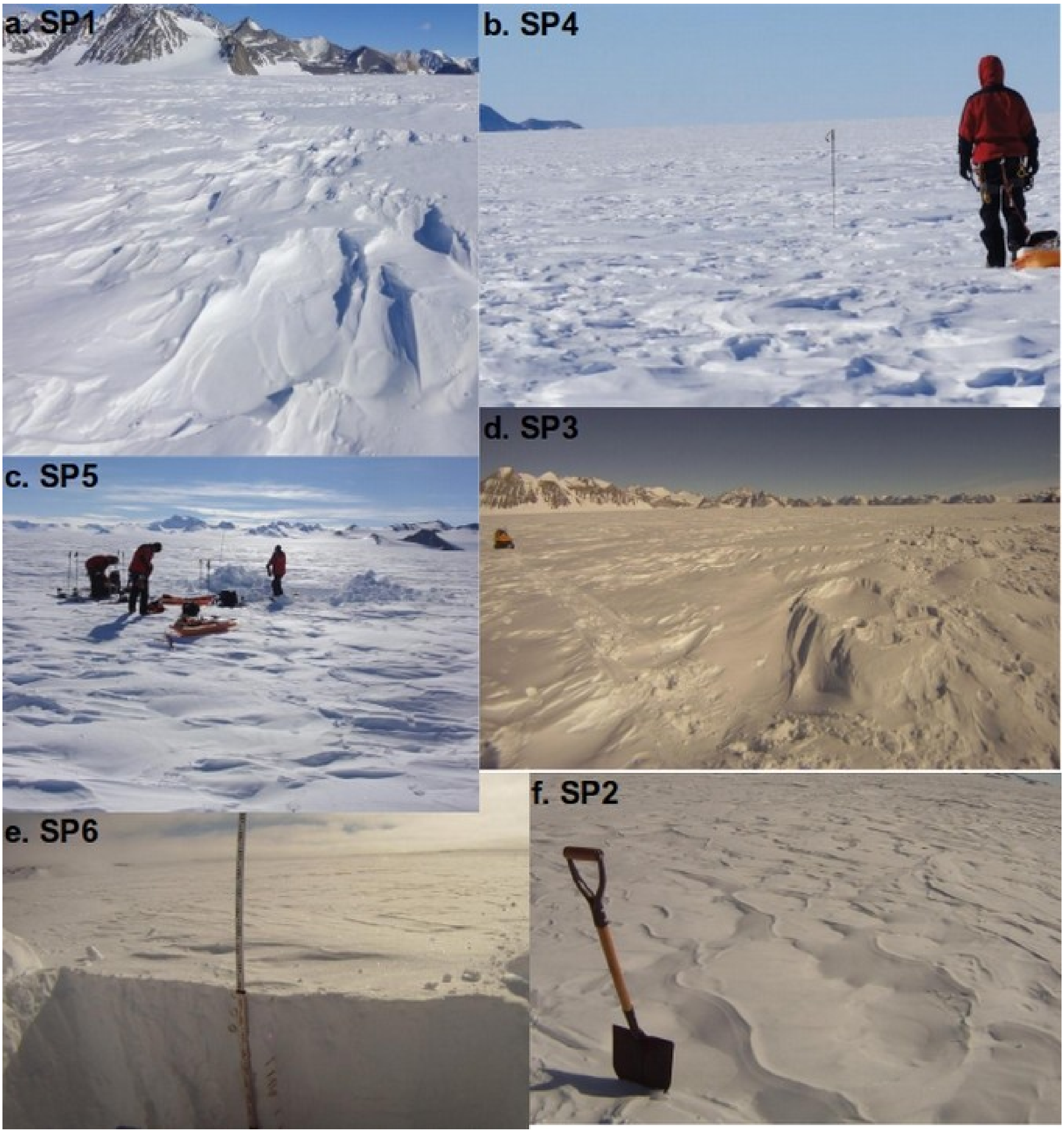

Figure 6: Pictures that were taken at each snowpit site at the time the snowpits were dug. We selected one picture of each snowpit to illustrate the surface relief. At the top, a. and b. show the erosion pit. In the middle, c. and d. show depositional-form patches and pits as redistribution zones. At the bottom, e. and f. characterize the depositional form.

3.3. SAR

The mean SAR image showed backscatter contrasts in areas of snow (unmasked); we generally observed higher values in the central valley and lower values in the tributary valleys

(Figure 7). Around the runway at the largest BIA in the upper portion of the central valley, backscattering is low because of the increase in specular dispersion. The greater the difference in dielectric constants between the target and adjacent mediums (e.g., ice/air), the greater the reflection coefficient become. Although the BIA matched this low backscattering, spots with brighter values were observed, which could have been caused by (i.) a small amount of snow cover with a hard, dense crust or (ii.) lower ice albedo, which increases sublimation, causing a roughness surface with the same frequency range as the X-band (~3.5 cm), increasing diffuse scattering (Figure 8).

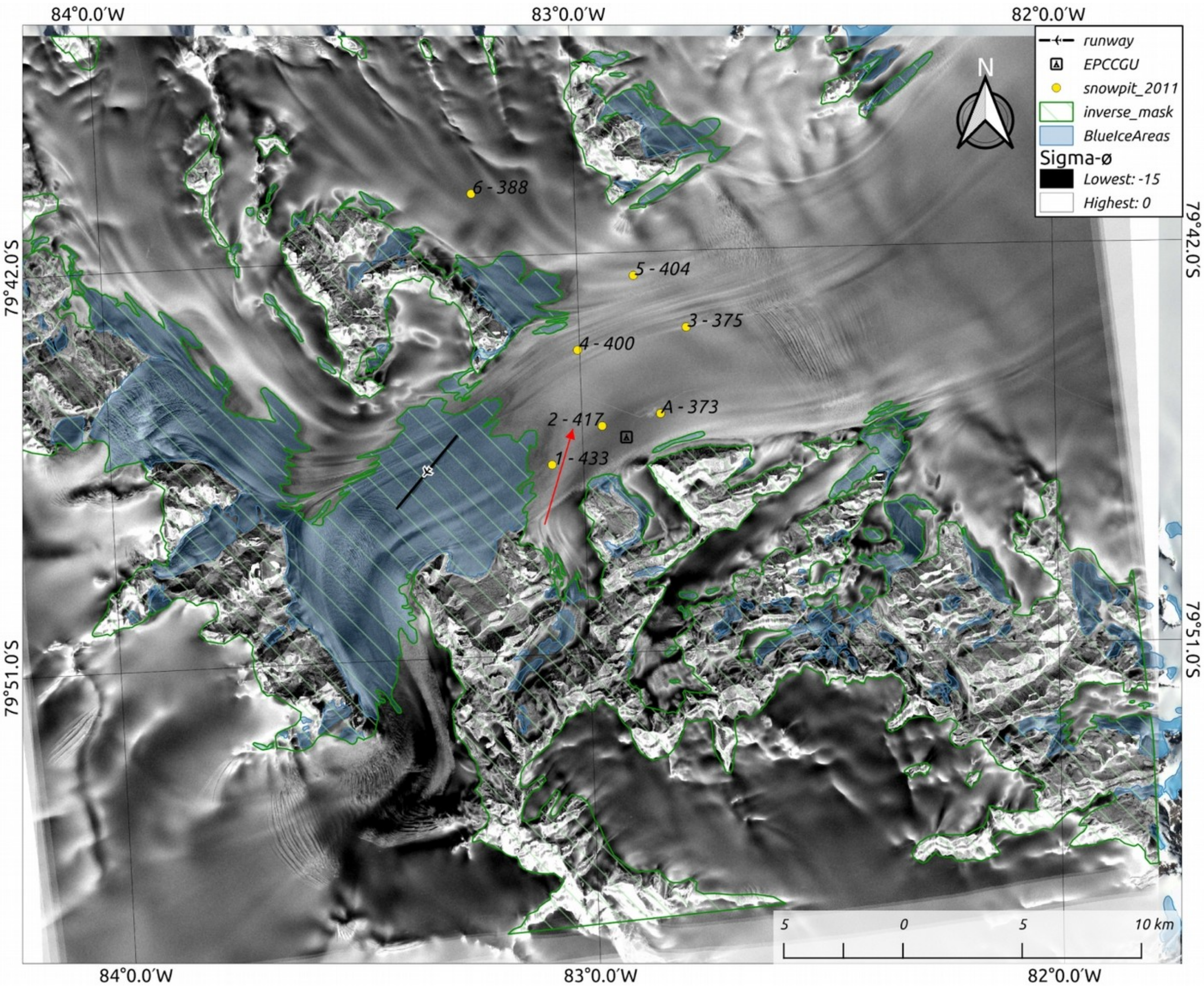

Figure 7: Averaged backscattering of the 5 VV COSMO-SkyMed images (Himage mode) that were used in the study. The final image was upscaled to 12-m resolution with a mean value. The green polygon corresponds to the masked area, and the blue dotted area inside the mask corresponds to BIA. The red arrow points to a brighter patch that appears to be a wind track that was forced by the topography. The image also shows the locations of the runway, the Chilean base camp, and the seven snowpit sites.

Figure 8: The surface roughness of the BIAs is 3.5 cm, which is the same scale as the X-band. Such a surface increase in diffuse scatter increases the backscattering signal more than a glazed ice surface, where specular scatter is dominant.

The SAR image was affected by the glacial flow structure, enhanced in the zone of ice-flow convergence of Union-Schanz and Union-Driscoll (covered by SP3 to SP5). On the left side of the central valley, lineation of the ice flux was evident. We compared simulated SAR images using the Reference Elevation Model of Antarctica (REMA) and the Tandem-X DEM. On the REMA simulated image, these lineation features were not observed (Figure 9a), while these features in the Tandem-X simulated image were also enhanced (Figure 9b). REMA is constructed from stereoscopic DEMs, which are extracted from pairs of sub-meter (0.32 to 0.5 m)-resolution digital globe images and delivered at 8-m postings. Therefore, we can assume that these features are not surface relief and that the SAR backscattering probably responded to sub-surface features.

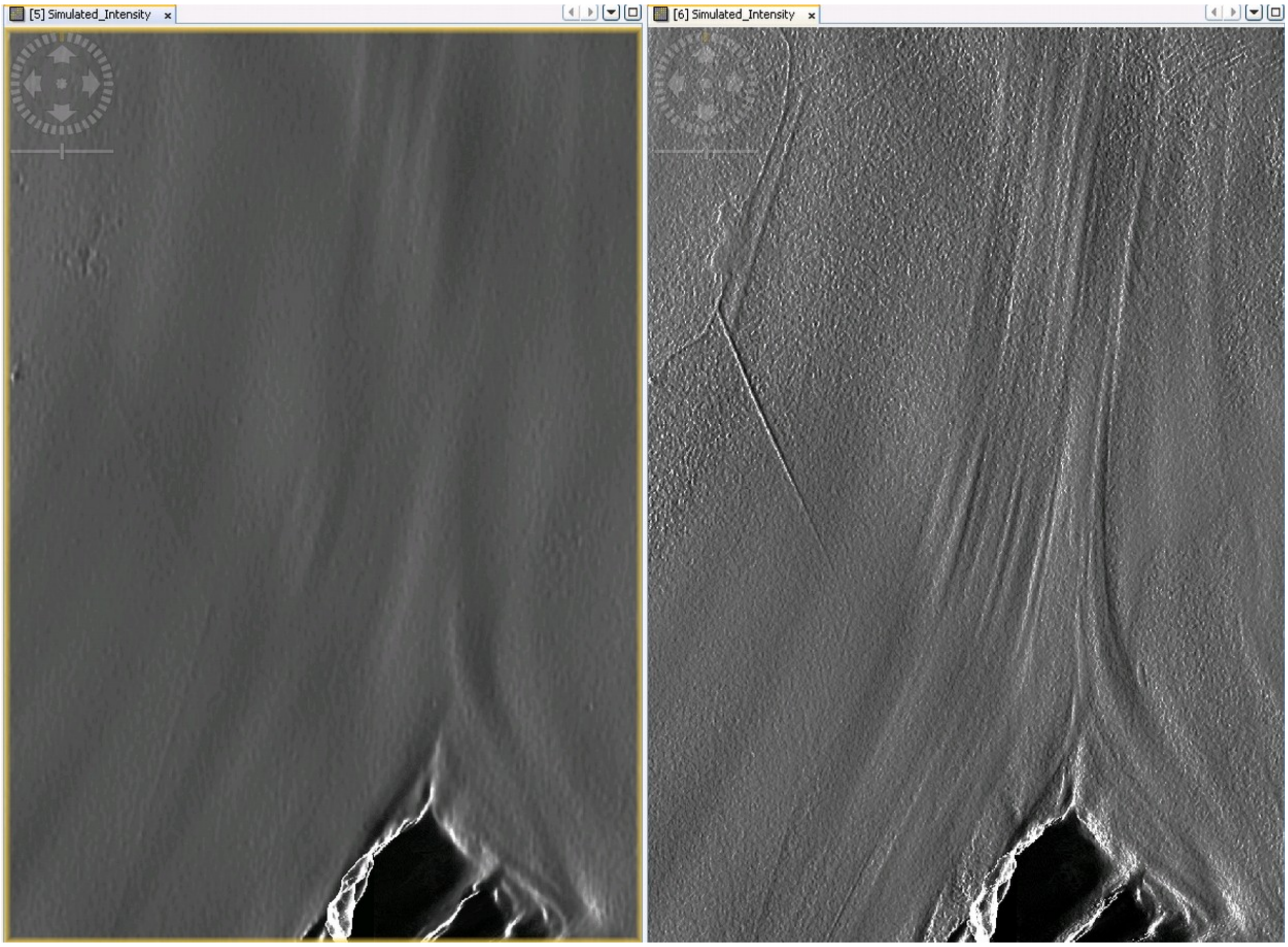

Figure 9: Simulated SAR images based on the REMA DEM (left) and TanDEM-X DEM (right).

Qualitative maps of the snow density and grain size provided a proper perspective on the differences in the snowpack characteristics (Figure 10 and Figure 11). Therefore, sites with high snow density also had larger snow-grain sizes. Higher temperature gradients favour constructive metamorphism with the development of faceted grains, whereas snow grains in the higher accumulation-rate zone in the first meter of the snowpack are smaller and increase in size with depth as the grains become rounded. The lowest density occurred at the high plateau, south of the mountain range at the bottom of the image, and inside the valley of the Schanz and Driscoll Glaciers in the wind-shaded zones. We observed higher densities in the main trunk of Union Glacier, while we observed intercalating patches of lower and higher densities transverse to the primary flux direction from the middle region downward to the grounding line (white rectangular box in Figure 10). These areas were related to changes in aspect windward/leeward, as will be shown later. We observed lower densities at the external boundary of the largest BIA in the central valley (black circles in Figure 10), characterizing a zone of higher accumulation rate that was associated with drift snow from the BIA and a positive downstream accumulation effect. We also observed a border of low density at the border of the BIA downstream from Driscoll valley. In contrast, the cross-polarized Ping Pong image (Figure 1) showed areas with the same backscattering as that inside the BIA, and the low backscattering was probably caused by a thin snowpack, reducing volume scattering and increasing surface scattering on the snow-ice boundary. A closest Landsat image was from 31 October confirmed snow cover in these areas and some BIAs. Leeward of Rossmann Mountain, we observed high-density snow, which was most likely associated with local wind blowing down the mountain alongside a low supply of mass because of the topographic shadow.

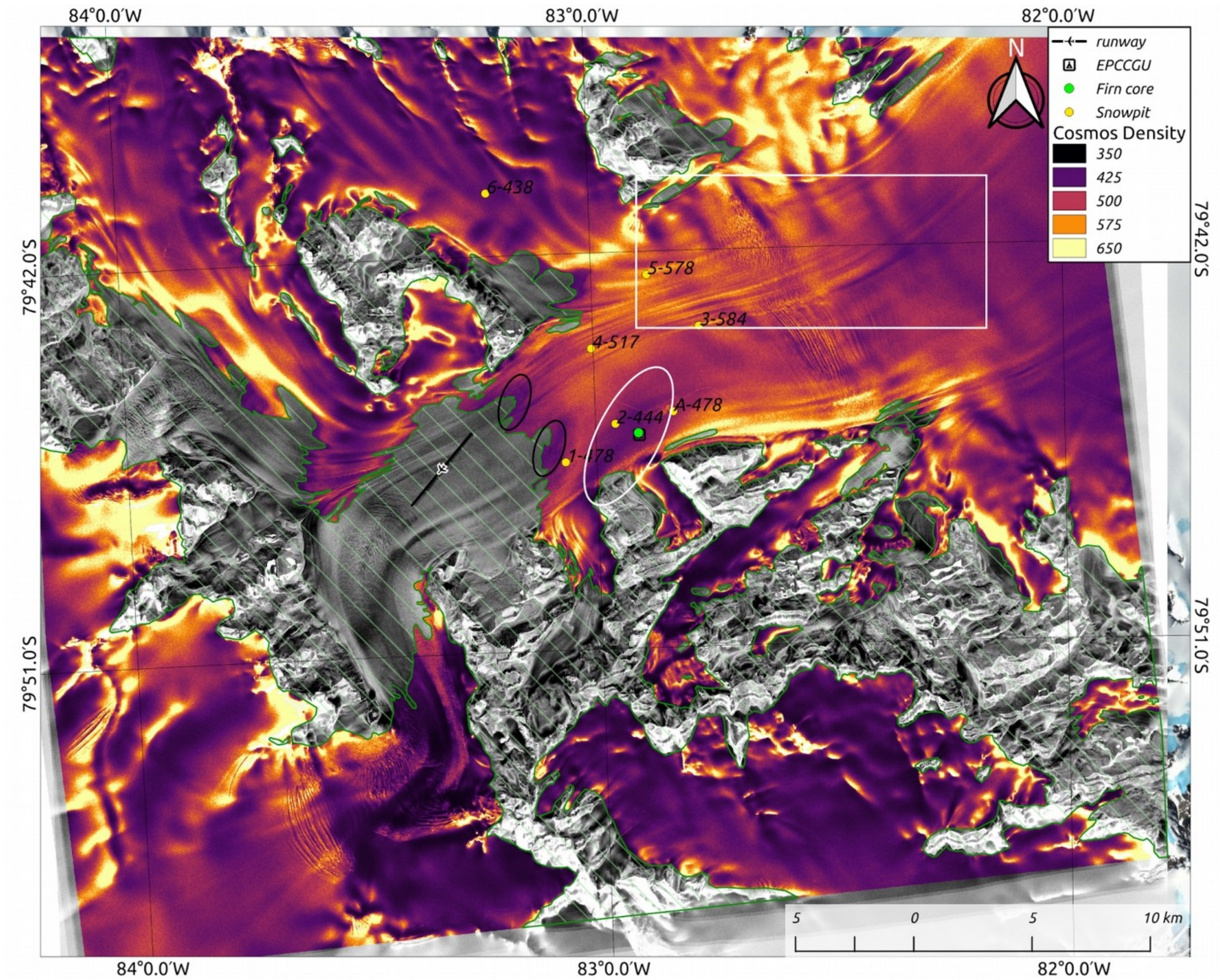

Figure 10: Map of the snow density that was derived with a radiative transfer model algorithm applied to each sigma image and then averaged and downsampled to 12-m resolution. The density corresponds to the average density of the first meters of snowpack where the X-band SAR signal interacts.

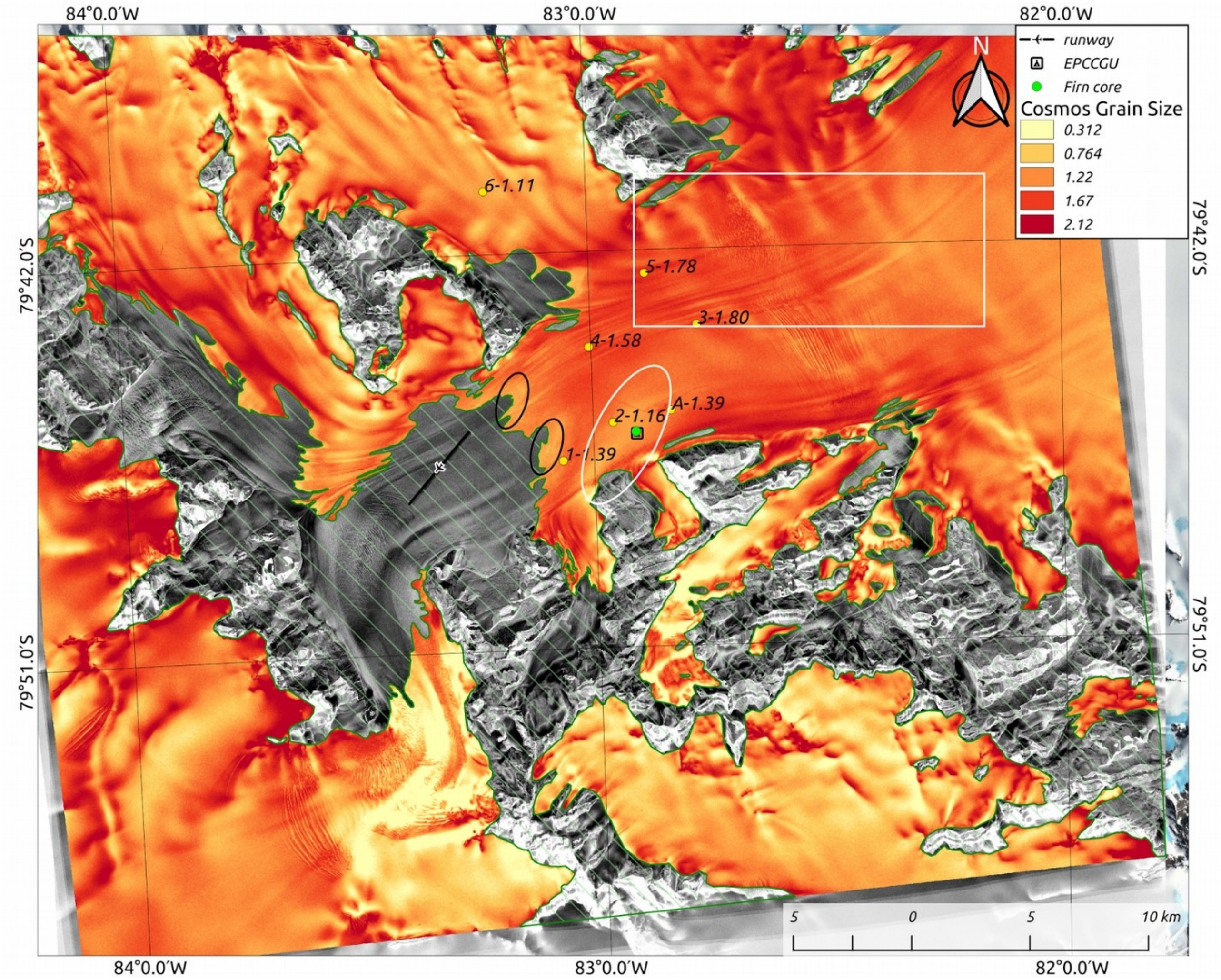

Figure 11: Map of the snow-grain sizes that was derived with a radiative transfer model algorithm applied to each sigma image and then averaged and downsampled to a 12-m resolution. The density corresponds to the averaged density of the first meters of snowpack where the X-band SAR signal interacts.

3.4. Terrain products

The four derived terrain products are presented in Figure 12, and the main interpretations are presented in the discussion section. The terrain aspect mainly affects the accumulation processes in two fashions. First, the terrain aspect determines the orientation aspect relative to the dominant wind direction. Second, the orientation relative to the Sun azimuth, where a Sun-faceted surface receives more radiation, affects the energy balance and temperature of the snowpack. The conversion of aspect from degrees to the land-surface aspect improved the cluster analysis because the 0º and 360º intervals are not oppose. The calculated slope reflected the surface microrelief from the high resolution of the DEM. In the considered area, the slope predominantly ranged between 1º and 3º degrees in the central valley. Higher values occurred at the boundaries with mountains, and some particular areas were associated with changes in bedrock topography. We used a colour map on a logarithmic scale (extracting the cubic root) and observed excellent agreement between the small change in low values of the slope with a contrasting change in the SAR image. We also extracted the cubic root for the surface roughness, as with the slope. The range of roughness values changed from 0-8 to 0.84-1.93 (Figure 12a.). The wind effect was generated from a 225º and 255º mean direction, and the 255º mean wind direction better represented the prevailing katabatic wind through the central valley (Figure 12b.).

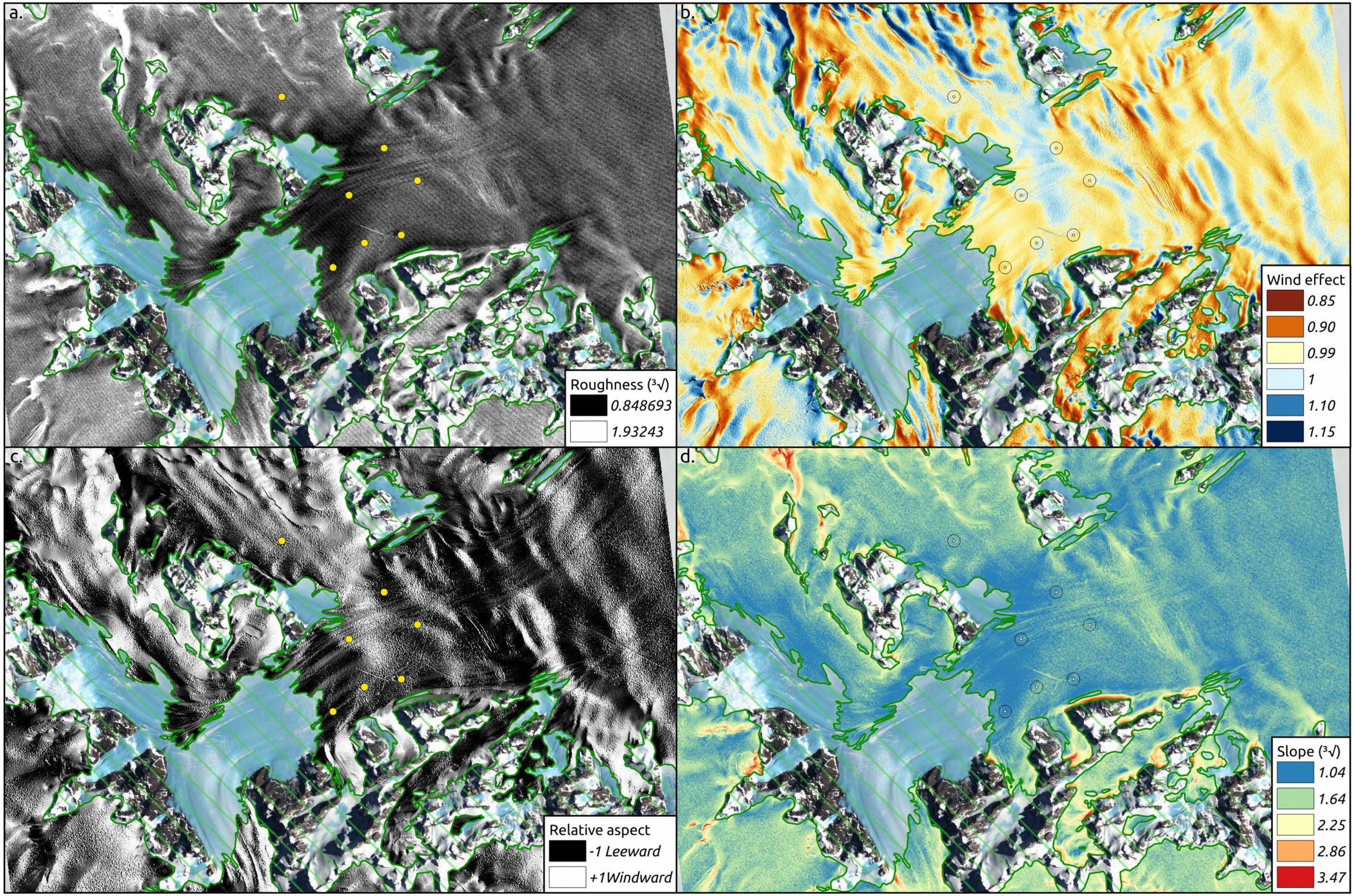

62Figure 12: Four derived terrain products: (a.) cube root of the roughness values; (b.) wind effect for a mean wind direction of 255º and search window of 1 km; values below 1 indicate wind-sheltered areas, and values above 1 indicate wind-exposed areas; (c.) cosine function of the relative aspect, where 1 indicates a windward orientation and -1 indicates a leeward orientation; and (d.) cube root of the terrain slope.

3.5. Cluster

In the first cluster classification, we used only the averaged sigma SAR image as input (Figure 13). We observed that the image basically separated classes between thresholds based on the intensity of the backscattering. The number of each class was random, and we reclassified them from low to high backscattering as zones with high to low accumulation rates, respectively, based on the transverse gradient in the "Criosfera Glacier". The first set of results classified SP5 and SP3 as lower accumulation-rate zones (orange). Both SP5 and SP3 were classified as lower rates than SP4 (yellow). However, SP3 and SP5 had high backscattering, but based on field knowledge and snowpit interpretations, we know that SP3 and SP5 had higher accumulation rates than more exposed wind zones, such as SP1 and SP4. Therefore, we focused on using the terrain products to explain the differences between these zones, as discussed above.

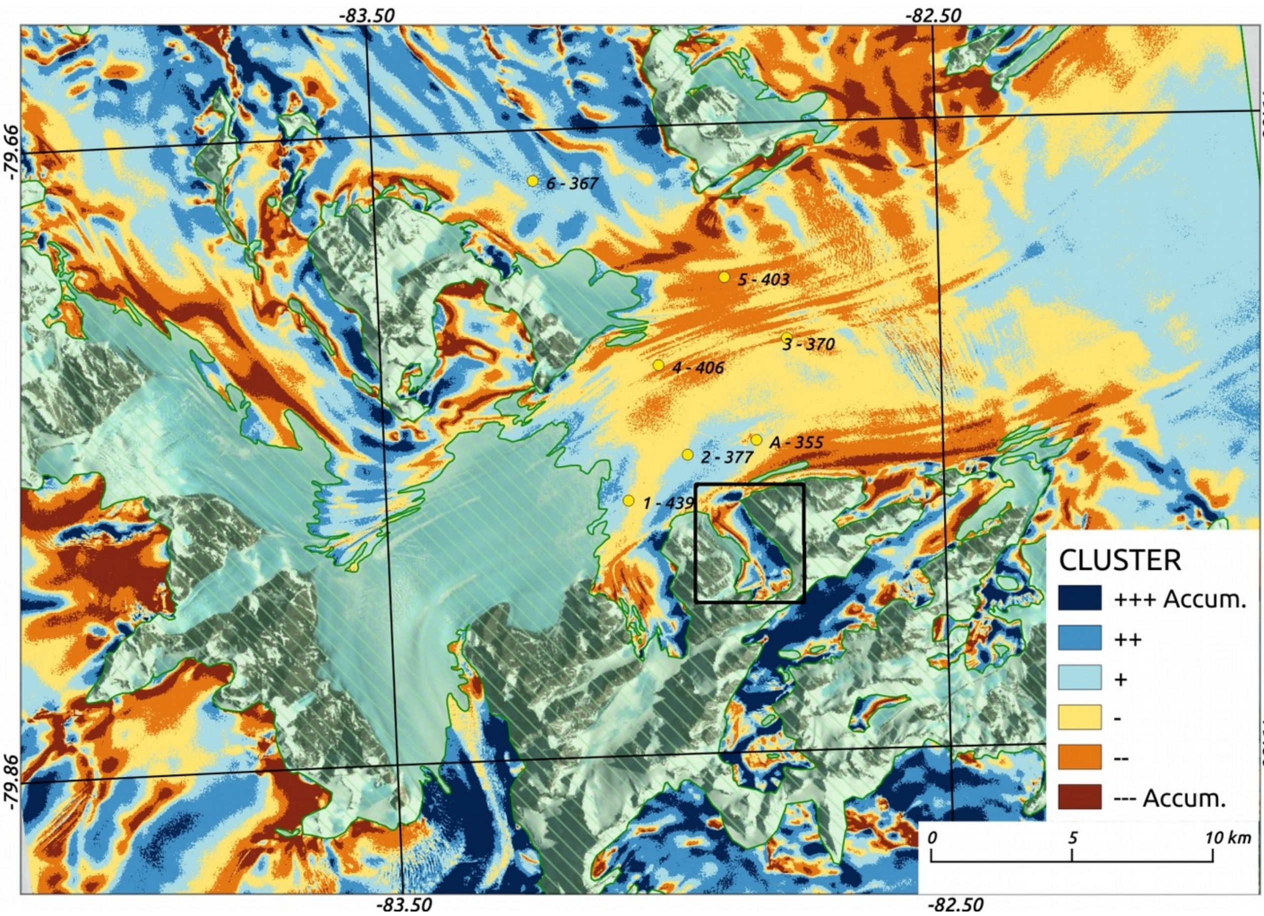

Figure 13: Cluster classification that was conducted with only the averaged sigma SAR image as input and six classes. The colour code is the relative accumulation rate between areas. We set the colours of each class based on the gradient from high- to low-accumulation areas at "Criosfera Glacier" (black rectangle).

In the second classification, we used the averaged SAR image alongside the four products of the terrain analysis. The results were improved, especially in terms of differentiating SP3 and SP5 from the deposition zone that corresponded to SP4. In the final classification (Figure 14), we observed a zone of generally low accumulation along the central valley, where we expect katabatic winds to have a greater influence. However, some patches of high-accumulation zones were driven by changes in surface characteristics, such as the roughness and wind exposure. We noticed that wind could influence areas that were sheltered from wind in two fashions: changes in the slope relief and aspect orientation to the dominant wind direction. Although the wind effect could indicate higher exposure to wind, this wind could have a positive effect on receiving blowing snow if a mass source was located upwind.